JACKSON, J. D. (1975). *Classical Electrodynamics*, 2nd ed. New York: Wiley.
JONA, F. & SHIRANE, G. (1962). *Ferroelectric Crystals*. New York: Pergamon.
KISLIUK, P. (1961). *Phys. Rev.* **122**, 405–417.
KLEINMAN, L. (1981). *Phys. Rev. B*, **24**, 7412–7414.
LANG, N. D. & KOHN, W. (1971). *Phys. Rev. B*, **3**, 1215–1228.
LASCHKAREW, W. E. & TSCHABAN, A. S. (1935). *Phys. Z Sowjetunion*, **8**, 240–254.
LAUE, M. VON (1948). *Materiewellen und ihre Interferenze*. Leipzig: Geest & Portig.
LU, Z. W. & ZUNGER, A. (1992). *Acta Cryst.* A**48**, 545–554.
MASLEN, E. N. (1988). *Acta Cryst.* A**44**, 33–37.
MIYAKE, S. (1940). *Proc. Phys. Math. Soc Jpn*, **22**, 666–676.
PENG, L.-M. & COWLEY, J. M. (1988). *Acta Cryst.* A**44**, 1–5.
PRICE, P. F., MASLEN, E. N. & MAIR, S. L. (1978). *Acta Cryst.* A**34**, 183–193.
REZ, P. (1978). *Acta Cryst.* A**34**, 48–51.
ROSENFELD, L. (1929). *Naturwissenschaften*, **17**, 49–50.
SANKEY, O. F. & NIKLEWSKI, D. J. (1989). *Phys. Rev. B*, **40**, 3979–3995.
SAUNDERS, V. R., FREYRIA-FAVA, C., DOVESI, R., SALASCO, L. & ROETTI, C. (1992). *Mol. Phys.* **77**, 629–665.
SHINOHARA, K. (1932). *Sci. Pap. Inst. Phys. Chem. Res. Tokyo*, **18**, 315–319.
SPACKMAN, M. A. (1986). *Acta Cryst.* A**42**, 271–281.
SPACKMAN, M. A. & STEWART, R. F. (1981). *Chemical Applications of Atomic and Molecular Electrostatic Potentials*, edited by P. POLITZER & D. G. TRUHLAR, pp. 407–425. New York: Plenum.
SPENCE, J. C. H. (1993). *Acta Cryst.* A**49**, 231–260.
SPENCE, J. C. H. & ZUO, J. M. (1992). *Electron Microdiffraction*. New York: Plenum.
STERN, R. M. & GERVAIS, A. (1969). *Surf. Sci.* **17**, 273–301.
STEWART, R. F. (1973). *J. Chem. Phys.* **58**, 1668–1676.
TAMM, I. (1932). *Phys. Rev.* **39**, 170–173.
THOMSON, G. P. & COCHRANE, W. (1939). *Theory and Practice of Electron Diffraction*. London: Macmillan.
THOMSON, G. P. & REID, A. (1927). *Nature (London)*, **119**, 890–895.
TONOMURA, A. (1987). *Rev. Mod. Phys.* **59**, 639–693.
TOSI, M. P. (1964). *Solid State Phys.* **16**, 1–120.
YADA, K., SHIBATA, K. & HIBI, T. (1973). *J. Electron Microsc.* **22**, 223–230.
YOSHIOKA, H. (1957). *J. Phys. Soc. Jpn*, **12**, 618–630.
ZUO, J. M., FOLEY, J. A., O'KEEFFE, M. & SPENCE, J. C. H. (1989). *Metal-Ceramic Interfaces*, edited by M. RUHLE, pp. 45–51. New York: Pergamon.
ZUO, J. M., SPENCE, J. C. H. & O'KEEFFE, M. (1988). *Phys. Rev. Lett.* **61**, 353–356.
ZUO, J. M., SPENCE, J. C. H. & O'KEEFFE, M. (1989). *Phys. Rev. Lett.* **62**, 2329.

Acta Cryst. (1994). A**50**, 45–52

The Calculation of Scattering Factors in HREM Image Simulation

BY D. TANG AND D. DORIGNAC

*CEMES-LOE/CNRS, BP*4347, 31055 *Toulouse CEDEX, France*

(*Received* 14 *December* 1992; *accepted* 3 *June* 1993)

Abstract

Two analytical approximations currently used for evaluating scattering factors for electrons, from a relativistic Hartree–Fock atomic potential and following the first Born approximation, are systematically studied. It is shown that their deviations from the scattering factors directly derived from the numerical Fourier transform of the potential vary with the spatial frequency and that these deviations are sufficiently large to introduce perceptible differences in the simulated image features, especially when strong multiple scattering occurs. In order to use better scattering factors and improve image interpretation, a new simple method combining both analytical approximations is suggested. For the first time, a more sophisticated atomic potential, a relativistic Hartree–Fock–Slater model, is also considered in the calculations. The importance of using accurate scattering factors in HREM image simulation is pointed out, particularly for future quantitative microscopy with the new ultra high resolution electron microscopes.

Introduction

In high-resolution electron microscopy (HREM), the calculation of atomic scattering factors for electrons is required for the interpretation of the images, which is based on comparison with computer simulations. The routine calculation is based on an analytical approximation: the scattering-factor curve is fitted to sums of several Gaussian functions of the form

$$f(g) = \sum_{i=1}^{n} a_i \exp(-b_i g^2/4) + c, \qquad (1)$$

where the coefficients a_i, b_i and c differ from one atom to another and g is the spatial frequency. With suitable scaling of the corresponding coefficients, $f(g)$ may be the scattering factor for electrons (f_e) or for X-rays (f_x) (Vand, Eiland & Pepinsky, 1957; Smith &

Burge, 1962; Doyle & Turner, 1968; Cromer & Waber, 1974). For the former, the calculated results can be used directly, but for the latter, which is more often employed, they must be converted by the Mott formula (Mott & Massey, 1965). The factors obtained by these methods are here called the E and X factors, respectively.

According to the first Born approximation, the fitting parameters described in (1) are based on the numerical Fourier transform of the atomic potential. Such a transform gives the scattering factor

$$f_e(g) = (8\pi^2 m_0 \gamma_0 e/h^2) \int_0^\infty r^2 \varphi(r)[\sin(2\pi gr)/2\pi gr]\mathrm{d}r, \quad (2)$$

which is generally considered to be a reliable representation of the true electron scattering factor, m_0 and e are the rest mass and the absolute value of the charge of an electron, h is Planck's constant, $\gamma_0 = (1 - v^2/c^2)^{-1/2}$ is the relativistic factor corresponding to the speed v of the incident electrons and $\varphi(r)$ is the atomic potential. These scattering factors will be referred to as RHF factors, as they have already been numerically computed and tabulated using a relativistic Hartree–Fock (RHF) atomic potential model (Doyle & Turner, 1968; Doyle & Cowley, 1974).

The Mott formula can be written as

$$f_e(g) = (m_0 \gamma_0 e^2/2\pi\varepsilon_0 h^2)[Z - f_x(g)]/g^2, \quad (3)$$

where Z is the atomic number and ε_0 the permittivity of the vacuum. Equation (3) will be divergent at $g = 0$ if an analytical approximation of $f_x(g)$ that does not tend to Z as g goes to zero is used. A convergent form of the Mott formula based on the analytical expression of (1) and the requirement that $f_x(0) = Z$ can be written as

$$f_e(g) = \frac{m_0 \gamma_0 e^2}{2\pi\varepsilon_0 h^2} \sum_{i=1}^{n} a_i[1 - \exp(-b_i g^2/4)]/g^2, \quad (4)$$

with the limiting form

$$f_e(0) = \frac{m_0 \gamma_0 e^2}{8\pi\varepsilon_0 h^2} \sum_{i=1}^{n} a_i b_i. \quad (5)$$

The advantage of using X and E factors over RHF factors in HREM image simulation is clear: it is faster and more convenient to calculate a set of sums than the Fourier transform of an atomic potential, for which there is no analytical expression. Since the fitting parameters have been obtained by a non-linear least-squares fitting of the RHF factor (for the E factor) or of the corresponding X-ray scattering factor based on the RHF atomic wave functions (for the X factor), both the E and X factors are to some extent different from the theoretically considered true value.

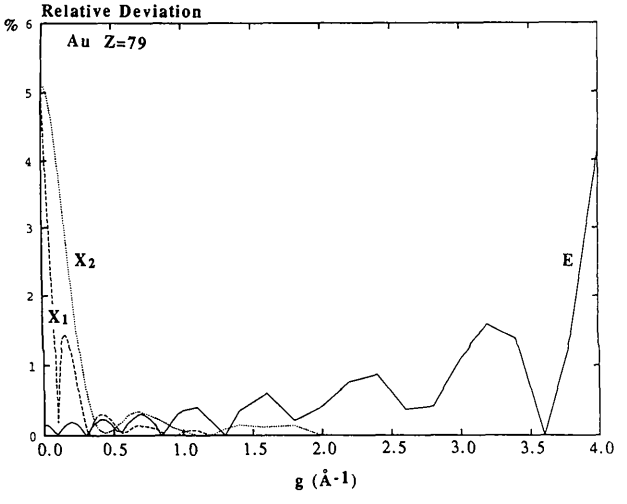

Fig. 1. Relative deviations of the E and X analytical approximations of the RHF atomic scattering factor for an Au atom as a function of the spatial frequency g. Note that the deviations for the two X factors, derived from two forms of the Mott formula, are greater in the low-g region and smaller in the high-g region than that for the E factor.

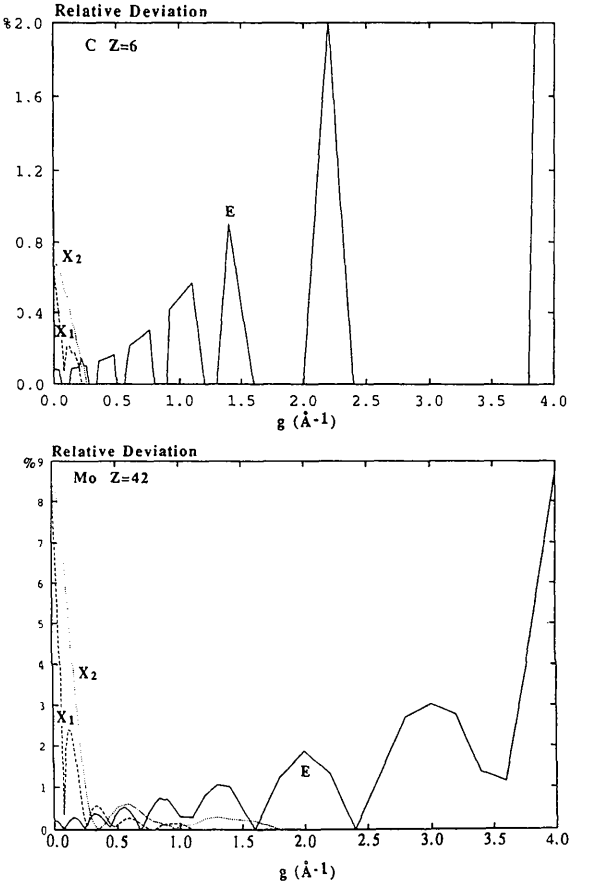

Fig. 2. Same curves as in Fig. 1 for C and Mo atoms illustrating that their behaviour is quite general for all atoms. For C atoms, the largest difference is 9% at $g = 4.0$ Å^{-1}.

Peng & Cowley (1988) have studied the difference between the X and E factors for an Au atom near $g=0$, showed the differences arising in the simulated HREM images of a gold crystal in the [110] orientation when it is very thick and demonstrated the possible misinterpretation of surface or other very large unit-cell-dimension structures by using X factors. They suggested avoiding the use of the Mott formula and employing the E factors in the simulation.

In the present work, the scattering factor of gold is also examined as an example. A mixed use of both E and X factors is proposed. This mixed factor gives rise to different diffraction patterns and hence different HREM image simulations, as confirmed by the multislice computing.

Scattering factors

Three relative deviation curves of the E and X scattering factors from the RHF factors for an Au atom are shown in Fig. 1, calculated from $g=0$ to $g=4.0$ Å^{-1}. Curve E refers to the E factor. Curve X_1 refers to the X factor obtained by (3), with the limitation of (5) as g goes to zero, and curve X_2 refers to the X factor but is derived from (4) and (5). Curves X_1 and X_2 are only different when g is smaller than 2.0 Å^{-1} and the latter is generally greater than the former. In other words, X_2 is generally worse than X_1, so that only X_1 will be considered henceforward and denoted by X. The figure shows that, in the region of low spatial frequencies, the relative differences between X and RHF values are greater than those for E values, arising from the divergence of the Mott formula, while the opposite is observed in the high-frequency region. This behaviour is not restricted to heavy atoms, such as Au atoms, but is quite general: see for comparison in Fig. 2 the corresponding curves for a light (C, $Z=6$) and an intermediate atom (Mo, $Z=42$).

It is not surprising to see such a big difference for the E factor as g is high. In Doyle & Turner's (1968)

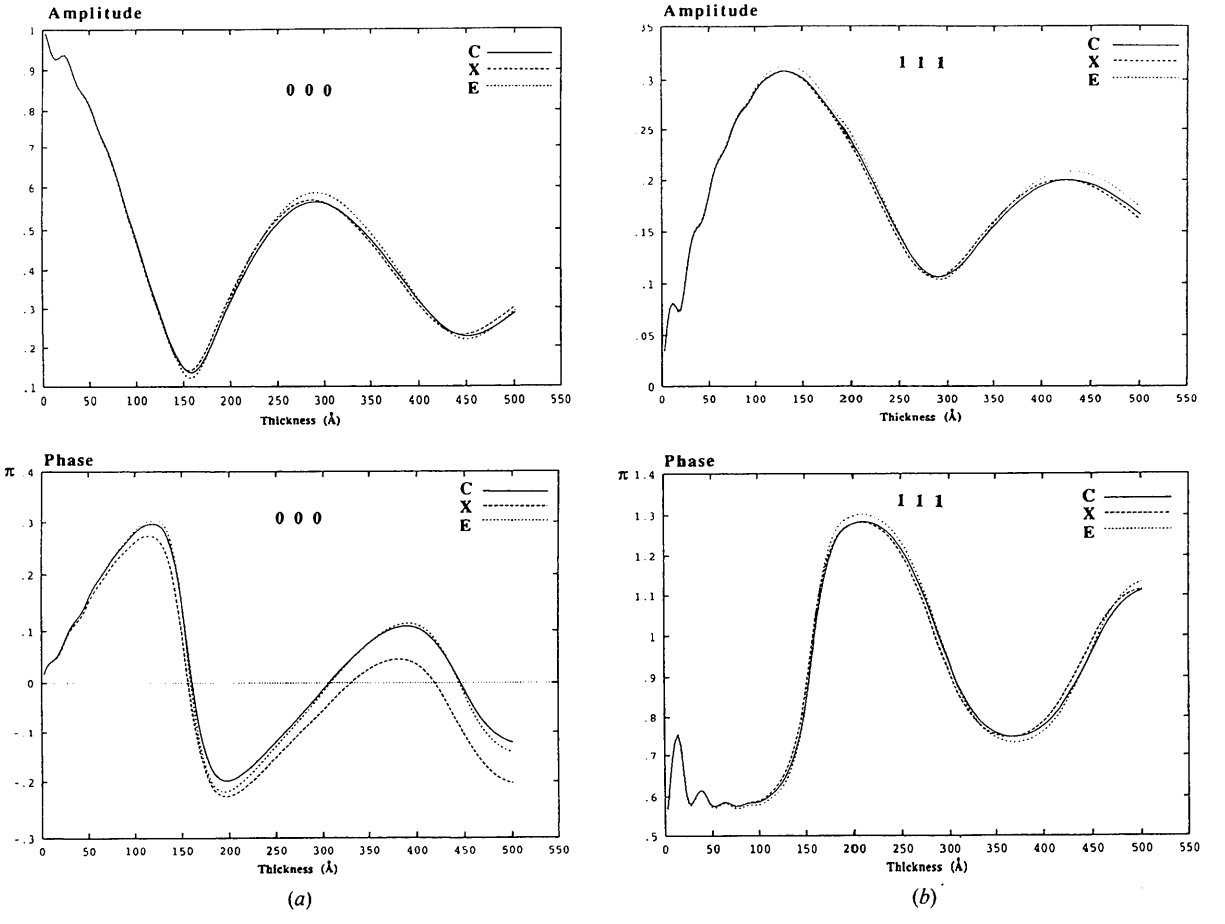

(a) (b)

Fig. 3. Dynamical calculated amplitudes and phases of (000) and (111) beams for a 300 keV electron wave function emerging from a gold crystal (⟨110⟩ orientation) as a function of its thickness. Three types of analytical approximation of the RHF scattering factor (E, X and C) have been used. The phases of (111) are relative to the corresponding (000) beam. Note that the differences for both amplitudes and phases are enhanced by the thickness effect.

original work on curve fitting, an error index, a root-mean-square value, defined as

$$[100/f(0)][\sum_{i=1}^{201} \delta_i^2/201]^{1/2},$$

has been tabulated for each element. Here δ_i is the deviation and 201 is the number of digital points in the range $g = 0.00$–4.00 Å^{-1} used for the curve-fitting procedure. The error indices for the f_x fitting, around 0.02 or less, are much smaller than those for the E-factor fitting, which are greater than 0.05 for most elements. Since the error for the E factor is smaller at low frequency, it must be greater in the other regions, although the error for the X factor is exag-

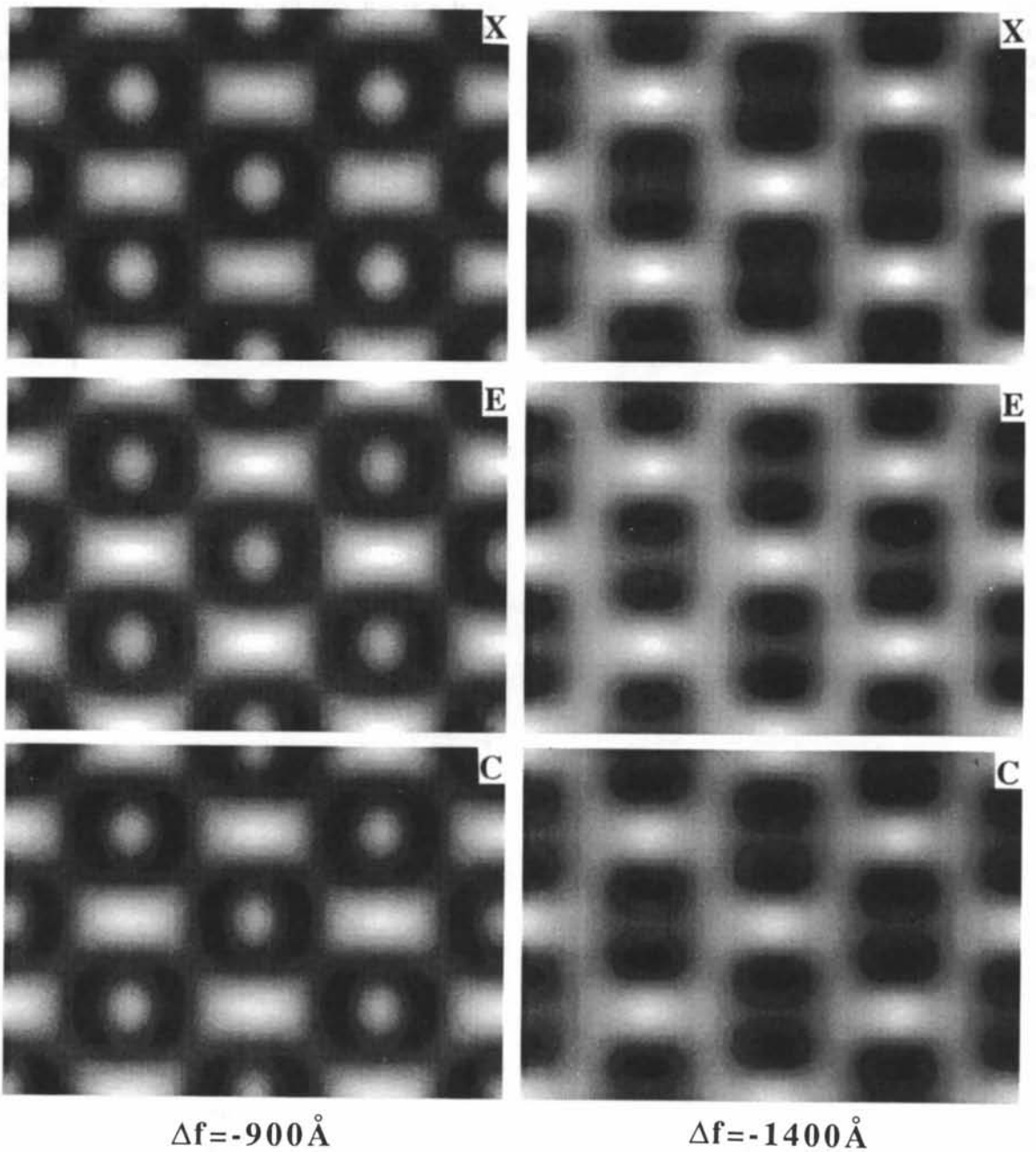

Fig. 4. Simulated images from RHF (X, E and C) scattering factors for an Au single crystal 300 Å thick in the ⟨110⟩ orientation with a 2×2 unit-cell projection using optical parameters suitable for a Philips CM30ST microscope ($C_s = 1.2$ mm, $R = 0.8$ Å^{-1}, $\Delta = 80$ Å, $\theta_c = 0.6$ mrad) and two defocus values. For visual comparison, an identical contrast level is set up for images with the same focus.

gerated in the small-g region and reduced in the large-g region by the presence of g^2 in the Mott formula.

The above results show that, for more accuracy, it is wise to use E factors in the region of low spatial frequencies, X factors in the region of high frequencies and either of them in the middle region. For an Au atom, for example, the E factor should be used from $g=0$ to 0.6 $Å^{-1}$, which is approximately the turning point of the relative deviation, and the X factor for other frequencies. In this way, the divergence of the Mott formula and the less-accurate fitting of the E factor are both avoided.

Exit wave field

The differences in atomic scattering factors, no matter how small they are, will certainly be reflected in the electron wave emerging from the object.

As an example, Fig. 3 gives the amplitudes and phases of the electron wave function at the exit plane of a gold crystal for (000) and (111) beams, with the ⟨110⟩ orientation, as a function of thickness [the phases of the (111) beam are relative to the corresponding (000) beam]. The values were calculated by a multislice program, *TEMPAS* (Kilaas & O'Keefe, 1989), modified for these special cases, assuming an incident plane wave with an energy of 300 keV and using three different analytical approximations for the scattering factors: the X and E factors already defined and a 'combined factor' (C) created by the method mentioned above, with the turning point 0.6 $Å^{-1}$, in order to minimize the errors arising from the use of X or E factors only. The enhancement of the differences in scattering factors by dynamical scattering through the crystal is clear, the curves being more split with an increase in thickness.

HREM image calculation

Appreciably different image features are thus expected for thicker crystals. If the simulated images for all three scattering factors are nearly identical, at least to the human eye, for thicknesses down to approximately 50–100 Å, extensive calculations over a wide range of defocus values show that differences in the images do become visible for thicker crystals.

For example, Fig. 4 gives the corresponding simulated images of a gold crystal in the ⟨110⟩ orientation for a 300 Å thickness, using 300 keV electrons and optical parameters suitable for a Philips CM30ST microscope (spherical aberration coefficient C_s = 1.2 mm, r.m.s. defocus spread $\Delta = 80$ Å, incident-beam divergence half-angle $\theta_c = 0.6$ mrad, optical aperture for spatial frequencies down to R = 0.8 $Å^{-1}$). Two defocus values, $\Delta f = -900$ and -1400 Å, were used. The same contrast level was

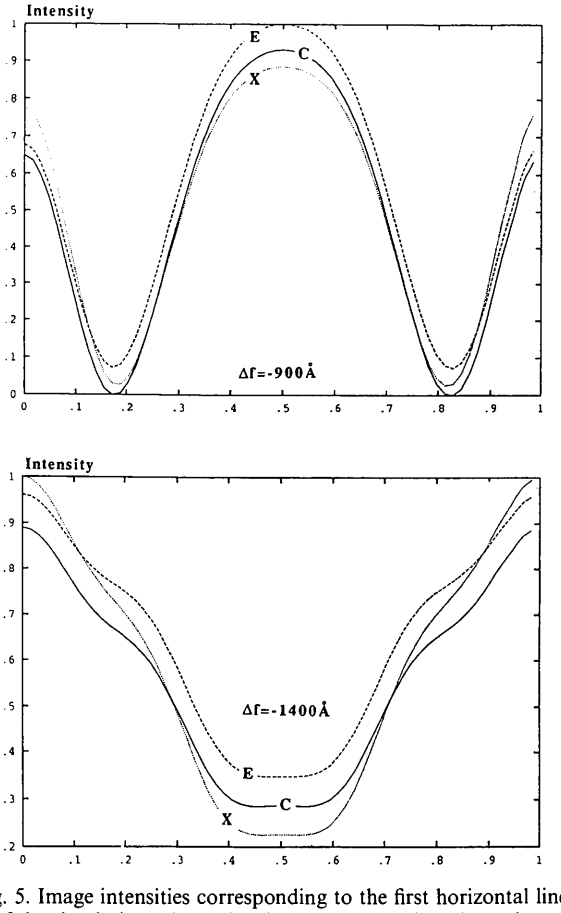

Fig. 5. Image intensities corresponding to the first horizontal lines of the simulations shown in Fig. 4 plotted against the real-space distance (taking the unit-cell dimension as a unit of length) to show quantitatively the image differences caused by the choice of different scattering factors.

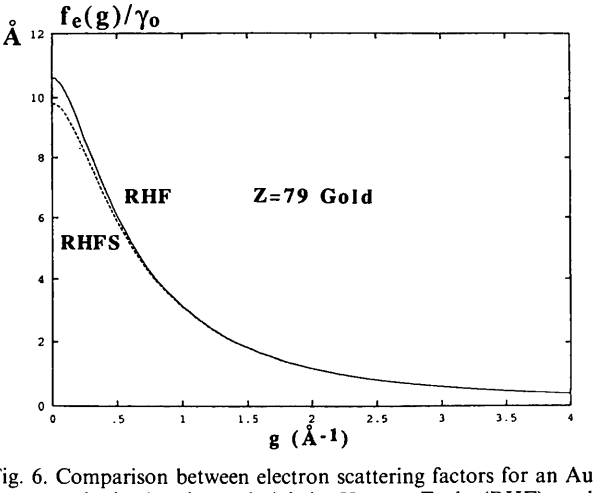

Fig. 6. Comparison between electron scattering factors for an Au atom obtained using relativistic Hartree–Fock (RHF) and relativistic Hartree–Fock–Slater (RHFS) atomic models (first Born approximation). They deviate notably when $g < 1.0$ $Å^{-1}$.

employed for three images with the same defocus value in order to compare them directly. To make matters clearer, the image intensities on the first horizontal lines of all the images are also plotted in Fig. 5 against the real-space distance, taking the unit-cell dimension as a unit of length.

The image-contrast differences, which are enhanced by dynamical multiple scattering through the crystal, confirm that different choices of electron scattering factors do lead to different simulation features. According to the analyses made above, the images computed using C factors are believed to be the best.

RHFS scattering factors

All the above calculations are based on the assumption that the RHF factors reliably represent the atomic world, although we know that the RHF model can be improved. A more sophisticated atomic potential, a relativistic Hartree–Fock–Slater (RHFS) model based on a self-consistent solution of the Dirac equation and tabulated for all elements from $Z = 2$ to $Z = 126$, with no less than eight decimal places and very fine steps (Carlson, Lu, Tucker, Nestor & Malik, 1970), has also been used to check the above results.

The RHFS factor, for which no analytical expression is available, has been computed directly by Fourier transformation of the potential. Fig. 6 gives a comparison with the RHF factor, tabulated by Doyle & Cowley (1974) for an Au atom, from $g = 0.0$ to $g = 4.0$ Å^{-1}: the RHFS factor is smaller than the RHF factor when $g < 1.0$ Å^{-1} simply because the correct treatment of relativistic effects leads to a significant improvement.

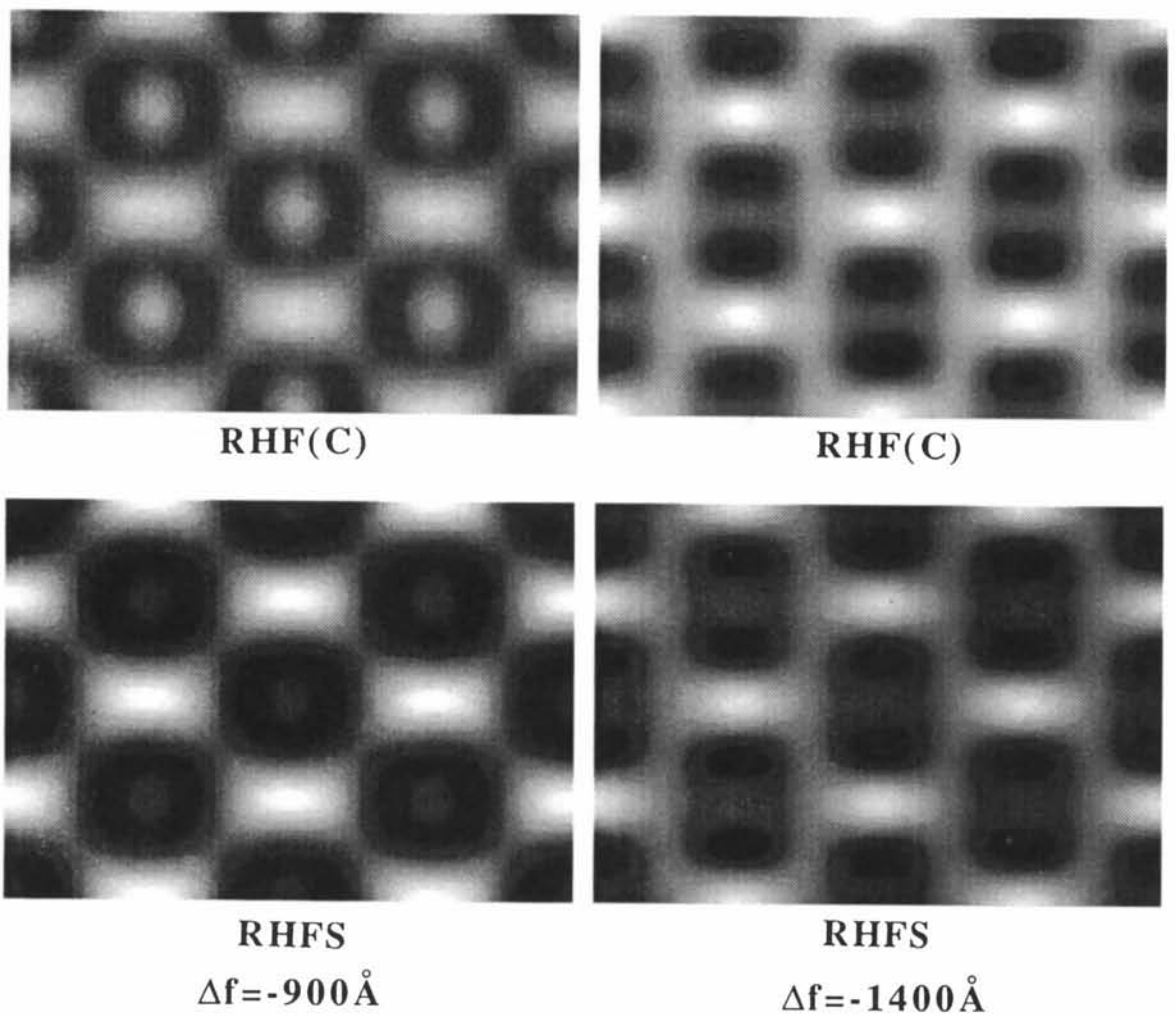

Fig. 7. The simulated images using the same parameters as in Fig. 4 for RHF (C approximation) and RHFS potentials.

Fig. 7 shows an example of the corresponding computer-simulated HREM images for a gold crystal 300 Å thick with the ⟨110⟩ orientation and using the same optical parameters as for Fig. 4. The same contrast level is selected for images with the same defocus value. The images for $\Delta f = -900$ Å are similar, although the RHFS image has a stronger contrast. However, for $\Delta f = -1400$ Å the contrast is reversed in such a way that there seems to be a half-unit-cell displacement along either the vertical or horizontal directions, as shown by the intensities plotted in Fig. 8. Of course, this latter case is an extreme result, especially chosen to demonstrate how important the image sensitivity *versus* the choice of the atomic potentials can be. However, the image differences over a wide range of (thickness/defocus) conditions remain generally smaller.

Discussion

Although the image differences caused by using RHF (*E*, *X* or *C*) or RHFS factors are not very large for single-crystal objects, they can still be observed and measured. These differences could be essential for detailed image interpretation of more complicated (defect) structures, for which the (defocus/thickness) series of the images are more sensitive to the structures. Moreover, for any meaningful quantitative measurement, it is very important to choose a scattering factor as accurate as possible. This concept of quantitative interpretation in electron microscopy has been proposed recently and, although it is still far from routine practice, some trials have been made in this direction (Hytch & Stobbs, 1992; Tang, Kirkland & Jefferson, 1993). It will certainly become more important in the near future.

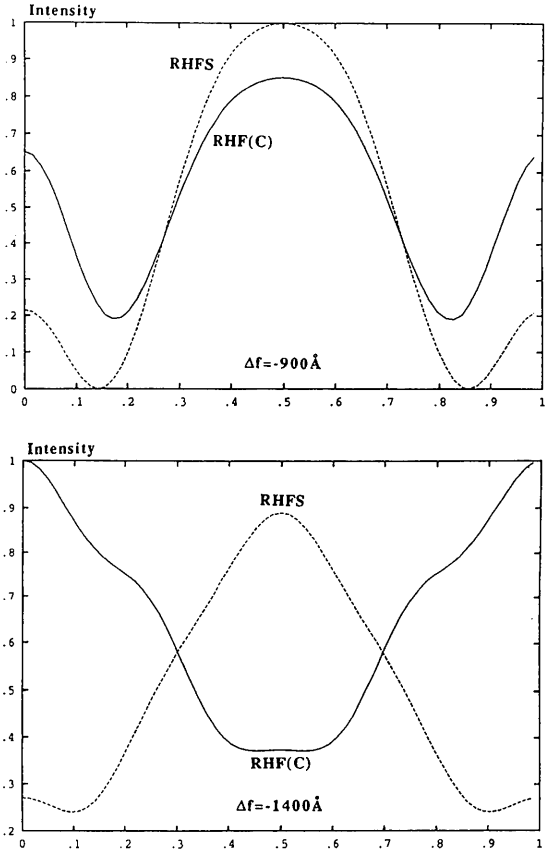

Fig. 8. Image intensities corresponding to the first horizontal lines of the simulations given in Fig. 7 with the same relationship as between Fig. 4 and Fig. 5.

It should be noticed that the use of only one turning point for the *C* factor, at $g = 0.6$ Å^{-1} for gold, may not be sufficient. Perhaps several turning points, where the *E* and *X* factors replace each other in turn, should be considered. The deviation of the *C* scattering factor from the RHF value could thereby be reduced further and the corresponding incorrectness of the simulated image would also be reduced.

It is interesting to note that both the *E* and the *X* factors are only valid from $g = 0.0$ to $g = 4.0$ Å^{-1} because Doyle's original work was based on curve fitting in this region. Generally, this is enough for a simulation with a point resolution around 2.0 Å. For microscopes with better performances, especially the new intermediate voltage instruments with field emission guns, capable of examining thicker samples, scattering factors of $g = 4.0$–12.0 Å^{-1} are required. At these higher scattering angles, Doyle's Gaussian fitting of f_x fails and no *E* factor is available but the new polynomial f_x fitting proposed by Fox, O'Keefe & Tabbernor (1989) can be used. Since the high value of g^2 will certainly reduce the error caused by the Mott formula in converting f_x to f_e, the latter and hence our proposed RHF(*C*) approximation will work better.

Concluding remarks

We have shown typical examples of different HREM simulated image features obtained with different electron scattering factors.

For better and more precise HREM simulations, we suggest using a combination of the direct analytical expressions for the RHF electron scattering factors and those of X-ray factors converted by the Mott formula rather than using them independently. Although this has little effect at small thicknesses, it does lead to remarkable differences for larger thicknesses.

The use of RHFS scattering factors, which are obviously more accurate than the more widely used

RHF expressions, can also lead to drastic differences at large thickness and, perhaps, far from the optimum underfocus condition.

To avoid uncertainties in image interpretation, a careful assessment of the scattering factors used should thus be made. When quantitative HREM is used to solve complicated structures, such as extended defects, these considerations will undoubtedly be necessary.

References

CARLSON, T. A., LU, T. T., TUCKER, T. C., NESTOR, C. W. & MALIK, F. B. (1970). Report ORNL-4614. Oak Ridge National Laboratory, Tennessee, USA.

CROMER, D. T. & WABER, J. T. (1974). *International Tables for X-ray Crystallography*, Vol. IV, Table 2.2*B*, pp. 99–101. Birmingham: Kynoch Press. (Present distributor Kluwer Academic Publishers, Dordrecht.)

DOYLE, P. A. & COWLEY, J. M. (1974). *International Tables for X-ray Crystallography*, Vol. IV, pp. 152–173. Birmingham: Kynoch Press. (Present distributor Kluwer Academic Publishers, Dordrecht.)

DOYLE, P. A. & TURNER, P. S. (1968). *Acta Cryst.* A**24**, 309–397.

FOX, A. G., O'KEEFE, M. A. & TABBERNOR, M. A. (1989). *Acta Cryst.* A**45**, 768–793.

HYTCH, M. J. & STOBBS, W. M. (1992). Proc. 32nd French Electron Microscopy Society Annual Meeting, Rouen, pp. 28–29.

KILAAS, R. & O'KEEFE, M. A. (1989). *Computer Simulation of Electron Microscope Diffraction and Images*, edited by W. KRAKOW & M. O'KEEFE, pp. 171–183. Warrendale: The Minerals, Metals & Materials Society.

MOTT, N. F. & MASSEY, H. S. W. (1965). *The Theory of Atomic Collisions*, 3rd ed., pp. 86–112. Oxford: Clarendon Press.

PENG, L.-M. & COWLEY, J. M. (1988). *Acta Cryst.* A**44**, 1–5.

SMITH, G. H. & BURGE, R. E. (1962). *Acta Cryst.* **15**, 182–186.

TANG, D., KIRKLAND, A. I. & JEFFERSON, D. A. (1993). *Ultramicroscopy*, **48**, 321–331.

VAND, V., EILAND, T. F. & PEPINSKY, R. (1957). *Acta Cryst.* **10**, 303–306.

Acta Cryst. (1994). A**50**, 52–55

Phase Determination from X-ray Powder Diffraction Data. II. Partial Patterson Maps and the Localization of Anomalously Scattering Atoms

BY W. PRANDL

Institut für Kristallographie, Universität Tübingen, Charlottenstrasse 33, *D*-72070 *Tübingen, Germany*

(*Received* 22 *March* 1993; *accepted* 8 *June* 1993)

Abstract

Partial Patterson maps containing peaks from anomalous scatterers only can be derived from powder diffraction data. For each anomalous scatterer, three data sets are needed: one off the edge and another two at two wavelengths close to the edge. The method presented is based essentially on the wavelength dependence of the real part of the anomalous scattering factor.

I. Introduction

Because of the high resolution of the X-ray diffractometers that are available now at many synchrotron sources, powder diffraction has become nearly equivalent to single-crystal methods: provided the resolution is high enough, individual intensities $I(\mathbf{H}) = |F(\mathbf{H})|^2 + |F(-\mathbf{H})|^2$ can be measured for a large number of reflections $\mathbf{H}$ and all the well established methods for the determination of crystal structures can then be used. This statement applies for wavelengths far enough from the absorption edges of atoms in the sample. If anomalous scattering comes into play, the coincidence of Bijvoet pairs in a powder diagram prevents the application of the well known single-crystal techniques, *e.g.* the multiple anomalous dispersion (MAD) method discussed by Karle (1980), for the determination of signs or phases.

In a previous communication (Prandl, 1990, hereinafter paper I), it was shown that, from a simple modification of the single-crystal algorithm, signs or phases can be obtained from powder data also, provided, as usual, the locations of the anomalous scatterers are known. We have demonstrated recently that signs can be determined uniquely in this way (Limper, Prandl & Wroblewski, 1991).

The main results of paper I may be summed up as follows. For the determination of signs, for centrosymmetric structures, a single anomalous scatterer is sufficient. Two data sets are needed, one with intensities $I_\sigma(\mathbf{H})$ close to the absorption edge of the atom σ and a second one with intensities $I_o(\mathbf{H})$ sufficiently far from the edge. In the acentric case, two different anomalous scatterers must be available in the structure. Three data sets are needed: one off all edges, $I_o(H)$, and another two close to the edges of the